Check for updates

Articles
doi.org/10.1002/batt.202000211

Chemistry Europe
European Chemical Societies Publishing

Investigation of Li Anode/FeS_2 Cathode Electrochemical Properties for Optimizing High-Power Thermal Batteries

Chae-Nam Im[+],[a] Chi Hun Choi[+],[a] Hye-Ryeon Yu,[a] Tae-Young Ahn,[a] Hyun-Ki Yoon,[a] Jae Seong Yeo,[a] and Jang-Hyeon Cho*[a]

Herein, the discharge properties of lithium (Li) anode with FeS_2 cathode system are investigated under different pressure loads, weight percent of Li, temperatures, and current densities to provide a fundamental understanding of the operational safety, electrochemical properties, and optimization parameters for Li anode-based thermal batteries. The lithium anode was prepared via physically mixing Li with Fe powder. The Li–Si alloy, the most common anode for thermal batteries, was investigated simultaneously to show the clear distinction in electrochemical performance between the Li anode and Li–Si anode. For achieving high operational safety and discharge performance with Li anode, the recommended pressure load and weight percent of Li are below 6 kgf cm^{-2} and 15 wt%, respectively, to prevent any leakage or short-circuiting problems. The discharge at 500 °C and 0.2–0.4 A cm^{-2} exhibits the optimal performance for the Li anode and FeS_2 cathode system. Finally, the thermal batteries with 17 cells are manufactured to confirm the aforementioned parameters at −32 and 63 °C to demonstrate that the previous results coincide with the actual battery level experiments. Due to the intertwined nature of the parameters, the optimization should always be conducted in a holistic manner to obtain high-performance thermal batteries for future military applications.

1. Introduction

Thermal batteries are specialized primary batteries typically used for defense applications including rockets, guided missiles, and torpedo. The major difference that distinguishes thermal batteries from other primary batteries such as lead-acid is that the thermal batteries require activation via pyrotechnic heat source. This activation generates sufficient heat to melt the initially insulating solid salt to highly conductive eutectic electrolyte to allow electrochemical discharge with high power output for a short duration of time. Owing to their inert, solid nature before activation, thermal batteries show a negligible self-discharge rate and high resistance toward temperature fluctuation, shock, vibration, and acceleration.[1]

Despite these advantages, current thermal batteries still have limitations that must be addressed and further optimized to satisfy the ever increasing energy requirements of future defense technology while abiding to the MIL-STD 810 requirements. Especially, in order to increase the battery performance for sophisticated weapons that require high pulse power or long mission time, the materials that can deliver more efficient electrochemical performance must be considered. Currently, the most widely used anode material is Li–Si alloy with the chemical formula of $Li_{13}Si_4$ (44 wt% of lithium) due to its high thermal stability, high lithium capacity, and superior performance than the Li–Al alloy. There are many other anode materials such as Li–B, Li–Sn, Li–Mg and other ternary alloys; however, so far, there have been limited attempts to investigate these materials in the actual battery-level experiments due to the difficulty of mass production, insufficient reliability, chemical instability, and cost.[2]

The major limitation that prevents Li–Si anode from being used in high-capacity, high-power thermal batteries is that Li–Si alloy undergoes a critical phase shift from $Li_{13}Si_4$ to Li_7Si_3 during discharge, which results in the undesirable voltage drop for about 0.15 V per cell.[2] The initial $Li_{13}Si_4$ phase only consists of approximately 30% of the total capacity required for Li–Si alloy to show a similar capacity to that of pure Li; thus, the anode has to be made significantly thicker, increasing the overall manufacturing cost and interfacial resistance between the electrodes. Also, since Li–Si is an alloy, the lithium ion must diffuse out from the alloy and travel to the cathode. This process inherently increases the internal resistance of the system, which is undesirable for high performance thermal batteries. To complicate the problem even further, the Li–Si anodes are created by a powder molding press technique. Li–Si alloy powder pellet shows low as-pressed density (1.0 g cm^{-3}) and insufficient mechanical strength; accordingly, the anode already has to be made unnecessarily thicker for handling purposes.

One of the possible solutions to solve the current limitation could be the utilization of pure lithium (Li) metal directly as anode. Li metal anode exhibits one of the highest theoretical capacity (~13,900 As g^{-1}), low redox potential (−3.04 V vs. SHE), and several other advantages such as mechanical durability when compared to Li–Si alloy. Li can be simply rolled to the

[a] C.-N. Im,[+] C. Hun Choi,[+] H.-R. Yu, T.-Y. Ahn, H.-K. Yoon, J. Seong Yeo, J.-H. Cho
Agency for Defense Development, Yuseong,
P.O. Box 35, Daejeon 34186, South Korea
E-mail: jhcho4535@naver.com

[+] These authors contributed equally.

Supporting information for this article is available on the WWW under https://doi.org/10.1002/batt.202000211

© 2020 Wiley-VCH GmbH

desired thickness and capacity, and the metallic nature allows simple handling to decrease the overall manufacturing cost with efficient material utilization. Li, however, also has obstacles that must be overcome to be used in the thermal battery applications: low melting point (180 °C), liquid nature during high-temperature discharge, and possible leakage that could lead to cell short circuit and catastrophic thermal runaway.

Catalytic Research Corporation developed the Li anode mixed with Fe powder as the physical binder to prevent Li leakage for the thermal battery application to overcome the aforementioned limitations. Due to the low melting point of Li metal, a significant amount of Fe powder (over 80 wt%) had to be added to increase operational safety of the thermal battery, which inherently decreased the specific energy of the anode. The iron powder is used because Fe is highly conductive and does not react with Li that the possibility of alloy formation is negligible. It should be emphasized that both wettability analysis done by Wang et al. and phase diagram suggest that these two materials are truly immiscible.[3] Therefore, numerous studies were performed to increase the operational safety and Li loading, typically with metal foams or porous materials. For example, Choi et al. recently demonstrated that the Fe powder binder could be effectively replaced with molten salt coated Ni metal foam.[4] The comparison between Li–Si anode and Li-impregnated metal foam anode (LIMFA) demonstrated the superior performance of LIMFA with high current density and voltage. Furthermore, a detailed thermal stability simulation with COMSOL Multiphysics software was conducted by Cho et al. to investigate the heat optimization parameters for thermal batteries made with Li and Li–Si anodes.[3d]

To build the thermal batteries with high reliability and credibility, however, the fundamental understanding of how the Li discharges at various conditions is essential. Furthermore, the Li and FeS_2 system should be considered simultaneously to explore the complete blueprint for thermal battery optimization. These previous studies, although important, are too-material-oriented and provide limited information regarding the underlying mechanisms and limitations. Despite efforts to inspect the electrochemical properties, the actual discharge analysis with FeS_2 cathode and the optimization of discharge characteristics under actual thermal battery operating conditions are limited. Briscoe et al. and Clark et al. from the ASB group reported the thermal battery performance of the pure Li anode compared to the Li–Si and Li–Al alloy systems. However, the information regarding the Li anode discharge characteristics under various conditions, limiting factors, operation, and safety are still unknown.[5]

In this study, the discharge characteristics of Li anode under various conditions were investigated with LiF–LiCl–LiBr electrolyte and FeS_2 cathode. The discharge profiles at different pressure loads, temperatures, and current densities were evaluated to demonstrate which parameters represent the limiting factors and how to optimize the Li anode for the thermal battery operation. The comparison between the electrochemical impedance spectroscopy (EIS) Nyquist plots was conducted to demonstrate the underlying mechanism of the thermal battery. With the acquired data, the actual thermal batteries with 17 cells were built and discharged at low (−32 °C) and high (63 °C) temperatures to validate the compiled results. This work should provide an intuitive understanding of the optimization of thermal batteries and their application in future military weapons.

Experimental Section

Preparation of Thermal Battery Electrodes and Thermal Batteries

The Li anode was prepared by physically mixing 13, 15, and 17 wt % of Li metal (Purity > 99.95 %) and 87, 85, 83 wt% of Fe powder (Purity > 99 %, particle size > 15 μm), respectively. The entire manufacturing process was performed in an Ar filled glove box with oxygen and water concentration less than 1 ppm. The physical mixing was conducted via a homemade blender on the heating mantle with the operating temperature at 350 °C. Li has poor wettability compared to other metal powders; thus, the physical mixing of these materials was carefully performed.[6] The Fe powder was put into the molten Li in five separate steps with more than 10 min of vigorous mixing in between the additions to ensure homogeneous dispersion in the molten Li. The final mixture was pressed on the alumina or graphite mold into an ingot, as shown in Figure 1A. The ingot was then roll-pressed and put into a Fe cup, the current collector (Figure 1B).

To compare the performance of pure Li anode, 75 wt% of Li–Si (44–56 wt%) alloy with 25 wt% of LiCl–KCl eutectic salt were mixed and pressed (powder molding technique) to prepare Li–Si anode. Similarly, for the cathode, 73.5 wt% of FeS_2 (Particle size ~98.6 μm, purity > 99 %), 25 wt% of a mixture of LiCl–KCl eutectic salt and MgO (65 wt%:35 wt%), 1.5 wt% of Li_2O (Purity > 97 %) were mixed and pressed to form the cathode as well. The amount of FeS_2 was determined with respect to the chemical reaction between Li and FeS_2. For the Z-phase transition, 1 mol of FeS_2 reacted with 1.5 mol of Li. Thus, the cathode was prepared so that the active material was slightly in excess to the mole ratio between Li and FeS_2. For electrolyte, 55 wt% of LiF–LiCl–LiBr eutectic salt and 45 wt% MgO (Purity > 99 %) binder were mixed and pressed with a similar method as mentioned above. The final single cell was assembled, as shown in Figure 1C, with Li anode, electrolyte, cathode, and current collector in sequential order. Finally, 17 battery cells were stacked under 4 $kgf\,cm^{-2}$ with appropriate thermal insulation around the cells to build the thermal batteries; they were discharged at low (−32 °C) and high (63 °C) temperatures to observe the discharge performances under harsh conditions.

Characterization and Experimental Discharge Conditions

The scanning electron microscopy (SEM) technique was used to analyze Li anode morphology, dispersion, and a cross-sectional view of the single cell before and after discharge. To observe the iron distribution more clearly in macro scale, micro X-ray fluorescence (XRF) spectroscopy was used to map 3.5 cm × 4.5 cm area of the anode. The beam spot size of the XRF was 20 μm, and the distance between the spots was 150 μm to map the designated area. The discharge apparatus was set to temperatures between 475 ~ 600 °C, and 3, 4, 6, or 10 $kgf\,cm^{-2}$ pressure was applied to imitate the operating condition of the thermal batteries. Each cell was placed for 3 min on the discharge apparatus, unless otherwise specified, at a variety of temperatures to ensure complete melting of the solid electrolyte and isotherm throughout the cell.

© 2020 Wiley-VCH GmbH

25666223, 2021, 2, Downloaded from https://chemistry-europe.onlinelibrary.wiley.com/doi/10.1002/batt.202000211 by University of Ulsan, Wiley Online Library on [11/11/2025]. See the Terms and Conditions (https://onlinelibrary.wiley.com/terms-and-conditions) on Wiley Online Library for rules of use; OA articles are governed by the applicable Creative Commons License

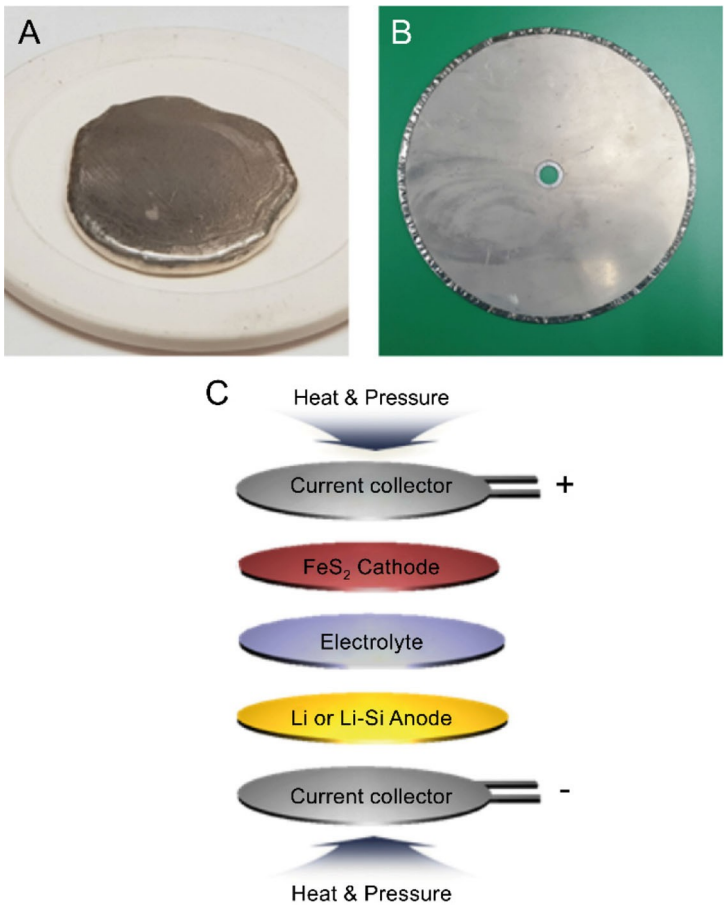

Figure 1. Li/Fe ingot (A), Li anode (B), and single-cell test assembly (C).

For the pulse sequence and EIS measurements, the cell was discharged with the pulse sequence of 0.4 A cm^{-2} for 1 min and 0 A cm^{-2} for 5 s as one cycle and continuously applied until the full discharge. For the subsequent experiment, the cells were discharged at current densities of 0.05–1.6 A cm^{-2} to investigate the differences in IR drop, power output, and general discharge characteristics. The ac impedance measurements were conducted over a frequency range from 50 kHz to 0.2 Hz with 10 mV peak-to-peak AC signal amplitude to measure the resistance change during the discharge and to obtain the EIS Nyquist plots. The pulse resistance (total polarization, R_t, Ω) was calculated by measuring open circuit voltage (V_{OCV}), closed circuit voltage (V_{CCV}), and current (I) [Eq. (1)]:[7]

$$R_t = (V_{OCV} - V_{CCV})/I \quad (1)$$

Finally, the thermal batteries were discharged under 0.3 A cm^{-2} current density at −32 °C and 63 °C. Except for the thermal battery discharge experiments, all the experiments were conducted in the dry room with the water level below 3 %.

2. Results and Discussion

2.1. Li Anode Microstructure Analysis

SEM was used to investigate the morphology of the Fe powder and as-processed pure Li anode. The initial Fe powder was a mixture of 10 μm-sized particles (Figure 2A) with some large aggregates (over 15 μm, Figure 2B). The microstructure of the as-processed pure Li anode is shown in Figure 2C–D. Due to the vigorous mixing procedure, the large aggregates were not observed in the final anode, suggesting that the shear stress during mechanical mixing diassembled the large Fe particle aggregates. Since Li cannot be detected via SEM and energy dispersive X-ray spectrometer (EDS) due to its low energy of characteristic radiation, determining the exact morphology of Li in the anode was not possible; therefore, the Li morphology was inferred via magnification. Figure 2C illustrates the ripples throughout the Fe network, suggesting that Li immobilization was successful and consistent throughout the Fe powder matrix. To pronounce the homogeneous distribution of Fe powder and Li, the backscattered electron (BSE) mode was used to provide a sharp contrast between two elements (Figure 2D). The contrast image demonstrates that the Li immobilization is uniform throughout the Fe powder network. Such distribution is necessary and highly desirable to minimize

© 2020 Wiley-VCH GmbH

25666223, 2021, 2, Downloaded from https://chemistry-europe.onlinelibrary.wiley.com/doi/10.1002/batt.202000211 by University of Ulsan, Wiley Online Library on [11/11/2025]. See the Terms and Conditions (https://onlinelibrary.wiley.com/terms-and-conditions) on Wiley Online Library for rules of use; OA articles are governed by the applicable Creative Commons License

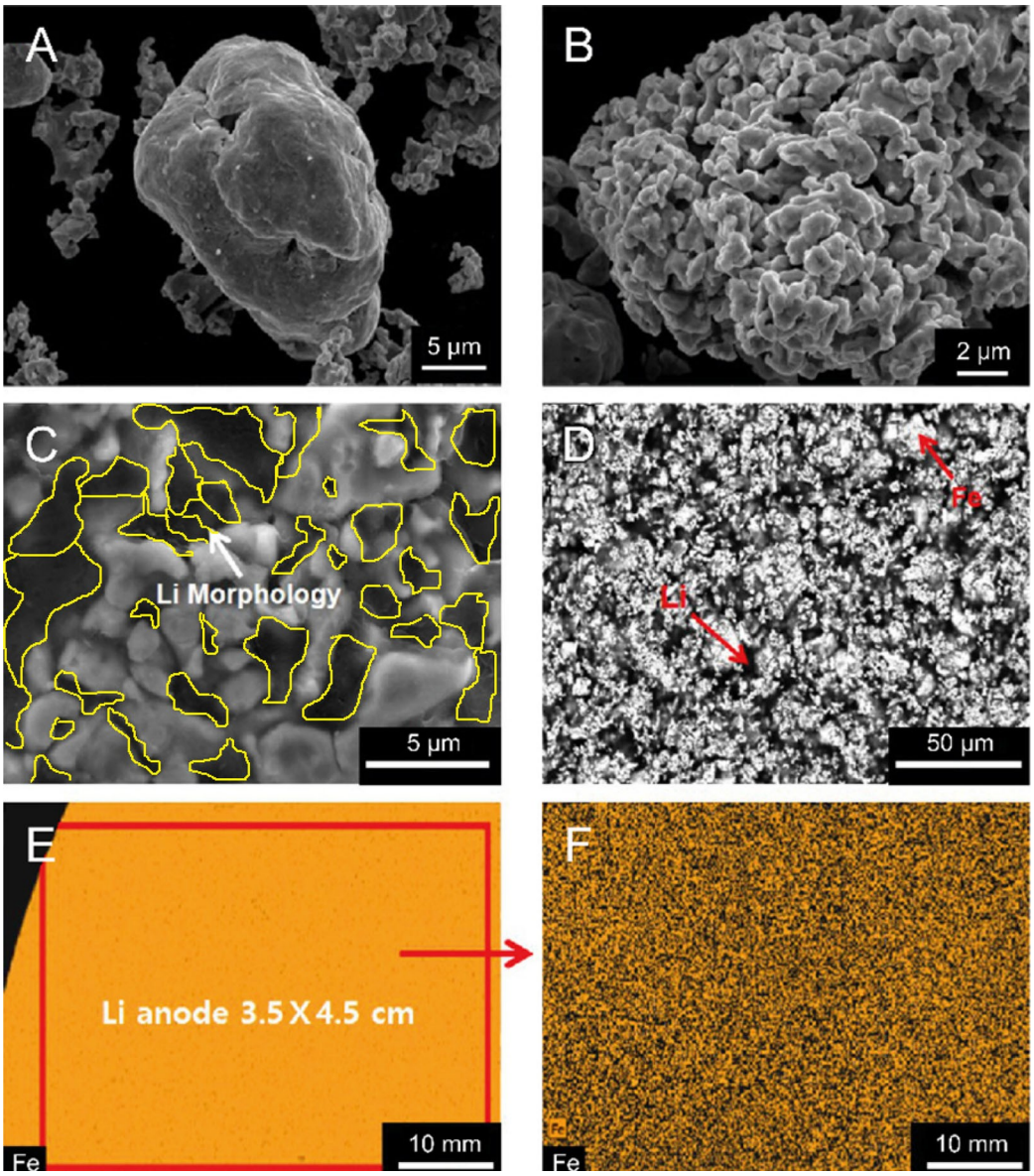

Figure 2. A, B) SEM image of Fe powder, C) SEM image of Li anode (lithium morphology denoted in yellow line), D) BSE image of Li anode (bright area: Fe, dark area: Li), E) micro-XRF mapping of the electrode (orange: Fe, dark area: Li), and F) zoomed-in version of the micro-XRF mapping of Fe in the anode

Li leakage during high-temperature discharge.[8] To ensure that the homogeneity is consistent throughout the anode, micro-XRF technique was employed to investigate the Fe distribution at macroscale level. Since Li is invisible in micro XRF as well, the dark spots are considered lithium, and Fe is denoted in orange (Figure 2E–F). As observed, the Fe powders are uniformly distributed throughout anode with no sign of agglomeration. Such a highly uniform distribution was possible only after applying the step-by-step addition of the Fe powder.

2.2. Applied Pressure and Weight Percent Dependence of the Discharge Performance

The optimization of applied pressure is considered as one of the critical elements for building efficient thermal batteries, so that the applied pressure can effectively decrease the interfacial resistance between the electrodes. Due to the *liquid* nature of Li during high-temperature discharge, the optimization of pressure is a crucial factor in ensuring not only ensure minimum interfacial resistance but also no leakage during discharge to prohibit cell short circuit and possible thermal runaway. To investigate how the change in applied pressure affects the aforementioned properties, the Li anodes with different weight percent of Li (13, 15, and 17 wt%) were tested under different pressure loads (3, 4, 6, and 10 $kgf\,cm^{-2}$).[9] The densities of the prepared anodes for 13, 15, and 17 wt% are 2.83, 2.57, 2.31 $g\,cm^{-3}$, respectively. These values are almost identical to the theoretical densities that the porosity of the anodes is not considered in this experiment.

The discharge performances of the 13 wt% Li anode (theoretical capacity: 1,807 $As\,g^{-1}$) and 15 wt% Li anode (theo-

© 2020 Wiley-VCH GmbH

25666223, 2021, 2, Downloaded from https://chemistry-europe.onlinelibrary.wiley.com/doi/10.1002/batt.202000211 by University of Ulsan, Wiley Online Library on [11/11/2025]. See the Terms and Conditions (https://onlinelibrary.wiley.com/terms-and-conditions) on Wiley Online Library for rules of use; OA articles are governed by the applicable Creative Commons License

retical capacity: 2,085 As g^{-1}) are shown in Figure 3A–B, respectively. Both 13 and 15 wt% Li anodes exhibited similar discharge curves for 3, 4, and 6 kgf cm^{-2} along with Li leakage at 10 kgf cm^{-2}. The degree of leakage, however, was much more severe when the weight percent of the Li anode increased to 17 wt% (theoretical capacity: 2,363 As g^{-1}) that even at 6 kgf cm^{-2}, as a significant leakage was observed (Figure 3C). Furthermore, the soft short circuit was observed at higher pressure load, resulting in lower discharge voltage and higher capacity loss for 17 wt% Li anode. The higher loading of Li, although beneficial for increasing capacity, is dangerous under applied pressure. This result is most likely due to the increased volume of Li. The 2 wt% increase in Li expanded the volume by 3.5%, implying that an insufficient amount of Fe binder is present per volume to inhibit the Li leakage. Thus, based on these results, the Li anode should contain 15 wt% Li or less, and the pressure should be 6 kgf cm^{-2} or less to ensure both excellent discharge performance and safety. In this case, we used 13 wt% Li anode and 4 kgf cm^{-2} as the applied pressure for future experiments.

To confirm that the above choice is correct, the discharge experiment of 13 wt% Li anode under 4 kgf cm^{-2} pressure without any bias (OCV condition) was conducted (shown in Figure 3D). The purpose of this experiment was to ensure the safety of the 13 wt% Li anodes under severe pressure loading conditions and to show that 4 kgf cm^{-2} is safe for thermal battery operation. The cell exhibited normal performance for 8,000 s without any leakage; the initial voltage drop was first observed at 5,700 s and continuously dropped afterward. To determine whether this phenomenon was due to Li depletion or leakage, the pressure was released at 6,150 s and re-applied at 6,180 s. As observed, the voltage was initially recovered to

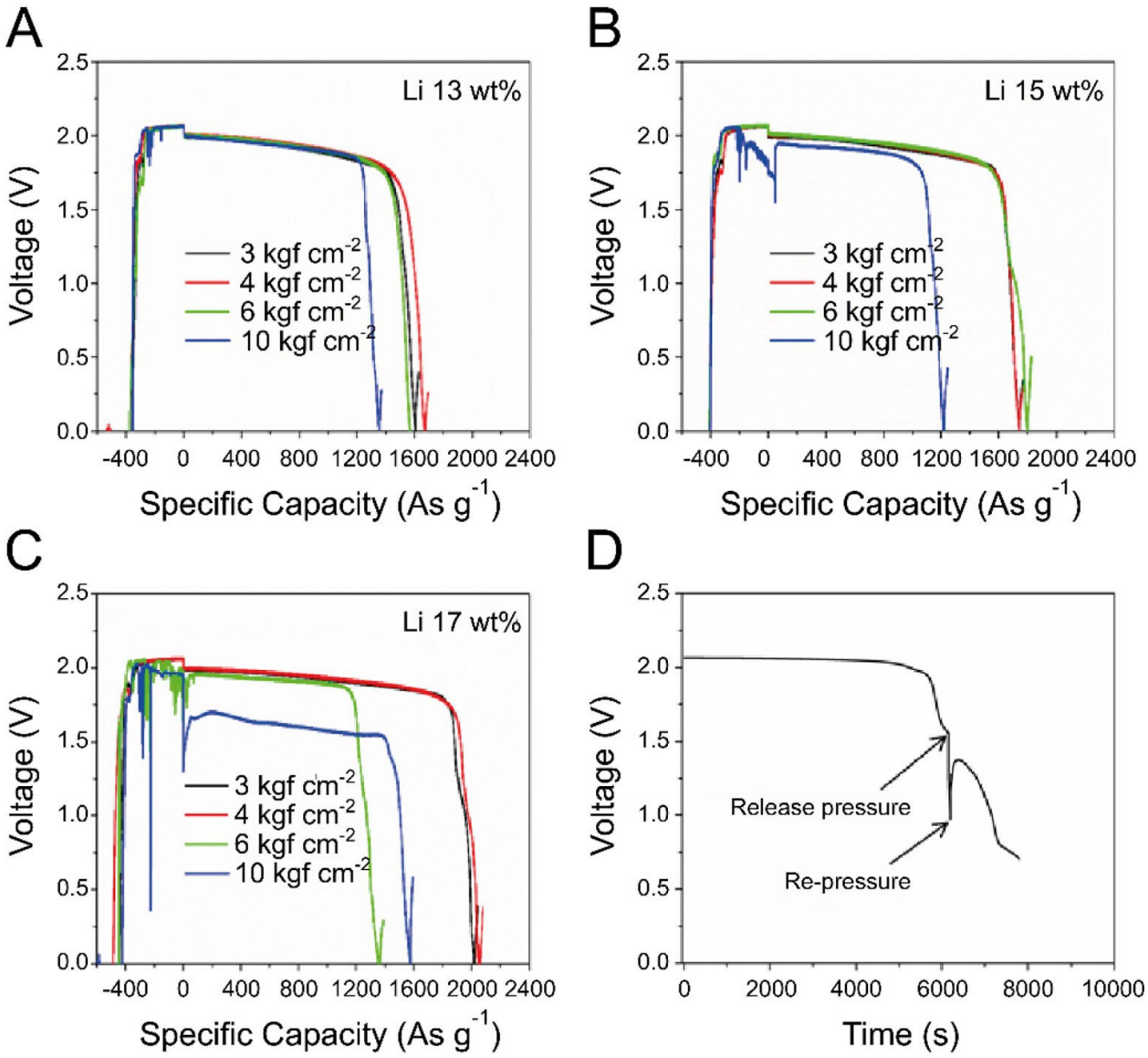

Figure 3. A) Discharge performance under different pressure loads of Li anode single cell with 13 wt% of Li, B) 15 wt%, C) 17 wt%, and D) open-circuit voltage with Li anode (Li 13 wt%) single cell under 6 kgf cm^{-2}

© 2020 Wiley-VCH GmbH

25666223, 2021, 2, Downloaded from https://chemistry-europe.onlinelibrary.wiley.com/doi/10.1002/batt.202000211 by University of Ulsan, Wiley Online Library on [11/11/2025]. See the Terms and Conditions (https://onlinelibrary.wiley.com/terms-and-conditions) on Wiley Online Library for rules of use; OA articles are governed by the applicable Creative Commons License

1.35 V but gradually dropped, implying that the voltage drop was caused by Li depletion rather than leakage or short circuit. This result indicates that the 13 wt% Li and 4 kgf cm^{-2} are safe and acceptable parameters for both safety and performance for thermal battery operation.

2.3. Temperature-Dependent Anode Performance in Thermal Battery Single Cell Discharge

The temperature is another important criterion that requires careful optimization for optimal and safe thermal battery performance because the temperature can influence the anode discharge performance, the ionic conductivity of the electrolyte, and cathode thermal stability. It is impossible to interpret how the temperature affects anode, cathode, or electrolyte individually due to the integrated nature of the thermal battery. Thus, this section focuses on analyzing how the temperature affects the entire Li/LiF–LiCl–LiBr/FeS_2 thermal battery system. Furthermore, the cathode used in this experiment was built with FeS_2 slightly in excess compared to Li to ensure the Z-phase utilization only and to exclude any additional electrochemical variable in the thermal battery.[10]

The discharge performances of the Li anode at different temperatures are shown in Figure 4A, with the specific capacity and Li utilization results summarized in Table 1. The specific capacities of the anodes were measured from OCV to cut-off voltage of 1.6 V at 0.4 A cm^{-2}. The obtained capacity values were then divided from the theoretical specific capacity, 1,807 As g^{-1}, to calculate the degree of Li utilization. The 13 wt% Li anode showed the highest performance at 500 °C with a specific capacity of 1,469 As g^{-1} (81.2% utilization) and lowest at 475 °C with a specific capacity of 1,301 As g^{-1} (72% utilization). Excluding the discharge result at 475 °C, the higher voltage was observed as the temperature was increased. The low performance observed at 475 °C could be explained with

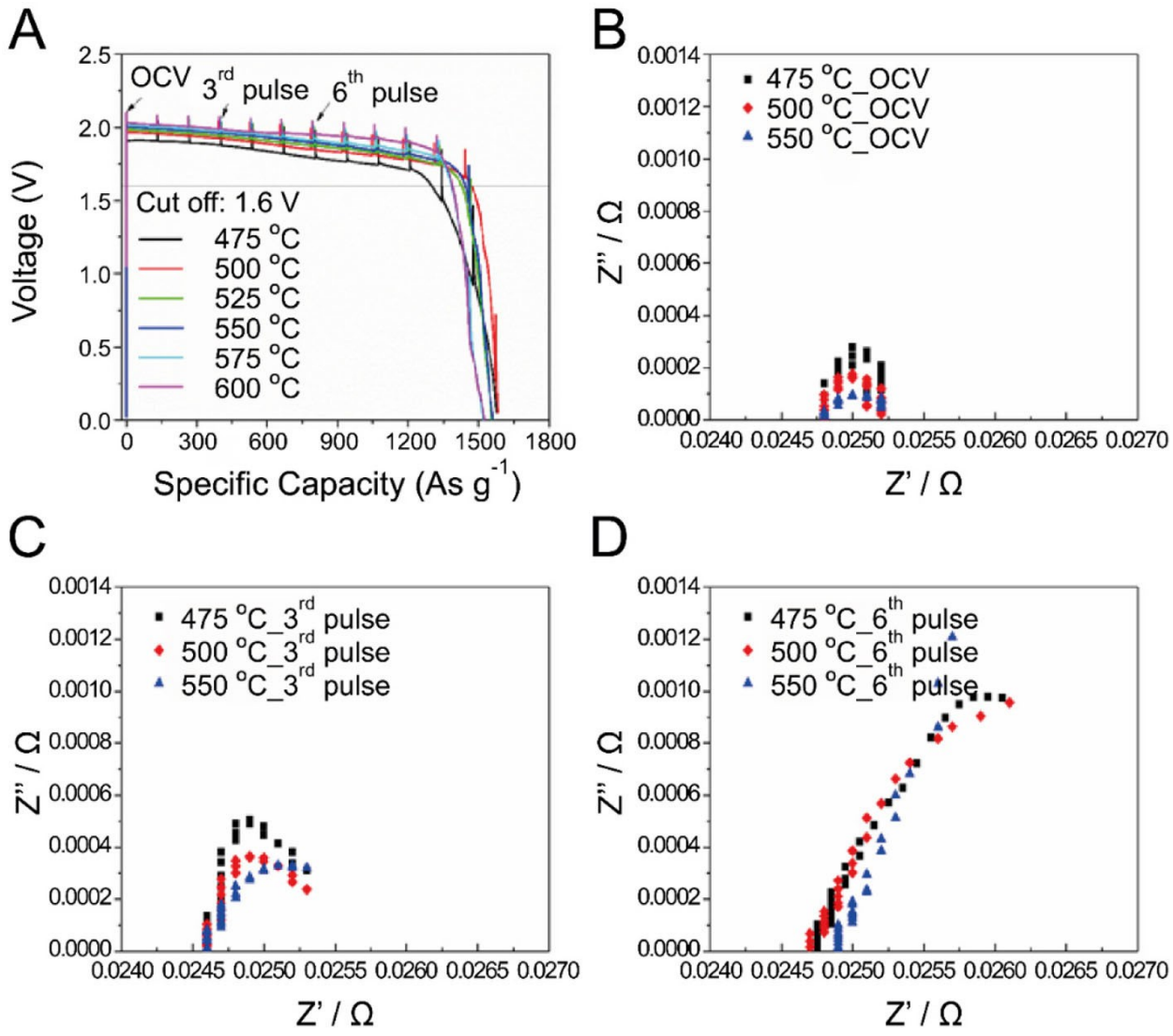

Figure 4. A) Discharge performance of Li/FeS_2 single cells under different temperatures (0.4 A cm^{-2} current density), B) EIS Nyquist plots for OCV, C) third pulse OCV, and D) sixth pulse OCV of Li/FeS_2 single cells.

© 2020 Wiley-VCH GmbH

25666223, 2021, 2, Downloaded from https://chemistry-europe.onlinelibrary.wiley.com/doi/10.1002/batt.202000211 by University of Ulsan, Wiley Online Library on [11/11/2025]. See the Terms and Conditions (https://onlinelibrary.wiley.com/terms-and-conditions) on Wiley Online Library for rules of use; OA articles are governed by the applicable Creative Commons License

25666223, 2021, 2, Downloaded from https://chemistry-europe.onlinelibrary.wiley.com/doi/10.1002/batt.202000211 by University of Ulsan, Wiley Online Library on [11/11/2025]. See the Terms and Conditions (https://onlinelibrary.wiley.com/terms-and-conditions) on Wiley Online Library for rules of use; OA articles are governed by the applicable Creative Commons License

Table 1. Specific capacity of Li/FeS_2 single cell with different temperature of cut-off voltage (1.6 V) at 0.4 A cm^{-2}.

	Temperature [°C]					
	475	500	525	550	575	600
Specific capacity [As g^{-1}]	1,301	1,469	1,432	1,443	1,386	1,386
Li capacity utilization [%]	72.0	81.2	79.2	79.8	76.7	76.7

the insufficient ionic conductivity of the electrolyte due to the high melting point of the LiF–LiCl–LiBr eutectic salt electrolyte, which is approximately 436 °C. It should be noted that the LiF–LiCl–LiBr eutectic salt electrolyte is relatively stable even in the presence of moisture and exhibits the highest ionic conductivity at the operating temperature. As the temperature rose, both OCV and voltage significantly increased due to high ionic conductivity (lower resistance) at the temperature over 500 °C.[10–11] The specific capacities, on the other hand, were comparable for the cells discharged at 500 and 550 °C, but experienced a sharp decrease under the temperature higher than 550 °C. The high temperature above 550 °C accelerated the decomposition reaction [Eq. (2)] of the cathode, and the self-discharge byproducts reacted with Li from the anode [Eq. (3)], which inherently decreased the overall capacity of the cell.[10,12]

$$FeS_2 \rightarrow FeS_{1.14}(s) + 0.43S_2(g) \quad (2)$$

$$FeS_2 \rightarrow Fe^{2+} + S_2^{2-} \quad (3)$$

The pulse resistances at first, third, and sixth pulses at different temperatures are summarized in Table 2. As shown, the pulse resistance decreases as the temperature is increased, coinciding with the aforementioned conclusion. To investigate the electrochemical discharge performance with respect to the different temperatures further, EIS Nyquist plots were obtained at OCV, third pulse, and sixth pulse for the cells discharged at 475, 500, and 550 °C. The direct comparison between the discharge performance and the EIS Nyquist plot was not possible due to the stabilization period given for the voltage fluctuation.

For OCV EIS measurement, all the cells were maintained at the desired temperatures for 15 min to ensure melting of the electrolyte and isothermal conditions to maintain steady open-circuit potential; for the third and sixth pulse, 15 min of recovery time was given to minimize the voltage fluctuation. Typically, the x-intercept correlates to the ohmic resistance arising from the cell assembly, active materials, and electrolyte. The semicircle region mainly attributes to the charge transfer impedance, and the linear region, although not observed for this experiment, is related to the Li-ion diffusion.[13] For the OCV and third pulse (Figure 4B–C), a decrease in the semicircular region with the temperature increment was observed with minimum change in ohmic resistance.

This result was expected as the higher voltage was observed at a higher temperature since the ionic conductivity was increased as the temperature was increased. Remarkably, for the sixth pulse in Figure 4D, the cell discharged at 550 °C showed not only higher ohmic resistance but also the largest semicircle radius. This result could be due to the prolonged exposure to heat that resulted in the degradation of FeS_2 cathode.

2.4. Current Density-Dependent Discharge Performance

The Li anode performance under various current densities was investigated to determine the optimal discharge conditions for the anode. The electrolyte and cathode used were identical to the experiments above, and the temperature was set at 500 °C based on the results derived from the previous section. The current density range was 0.05 to 1.6 A cm^{-2}, and the cut-off voltage was 1.6 V. In Figure 5, the discharge performances at various current densities are shown. As the current densities increased from 0.05 to 0.4 A cm^{-2}, the specific capacity and the Li utilization were increased. However, the sharp decrease in performance was observed as the current densities were increased from 0.8 to 1.6 A cm^{-2} with a significant IR drop. The IR drop was doubled from 0.4 to 0.8 A cm^{-2} and quadrupled from 0.4 to 1.6 A cm^{-2}. This result indicates that to discharge at such high current density is not recommended. Rather, it is more advantageous to increase the surface area of the electrode so that the overall current density is within the range between 0.2 and 0.4 A cm^{-2}.

Noteworthy, the low current density also resulted in the performance decrease. To observe this effect more clearly, the time profile must be considered to see the degree of degradation (Figure 5B). When comparing the cells discharged at 0.4 A cm^{-2} (815 s) and 0.2 A cm^{-2} (1,662 s), the time profile

Table 2. The pulse resistance (impedance) at different temperature during discharge.

Temperature [°C]	1st pulse [mΩ]	3rd pulse [mΩ]	6th pulse [mΩ]
475	1.68	3.02	3.38
500	1.54	2.36	2.48
525	1.52	2.18	2.23
550	1.38	1.84	1.95
575	1.29	1.70	1.84
600	1.16	1.68	1.68

© 2020 Wiley-VCH GmbH

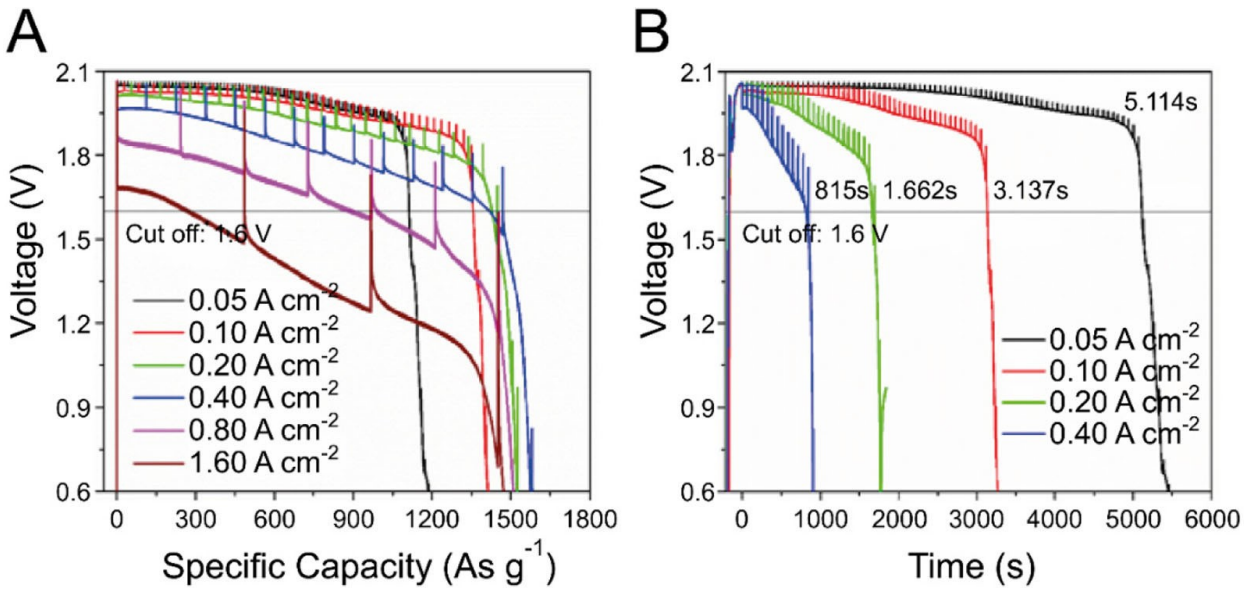

Figure 5. A) Specific capacity of Li/FeS_2 cells at different current densities and B) corresponding time profiles at 500 °C

difference was 2.04 times, an expected result because the current density was doubled. However, the cells discharged at 0.1 A cm^{-2} (3,137 s) and 0.2 A cm^{-2} (1,662 s) showed only 1.89 times difference; for the 0.05 A cm^{-2} (5,114 s) and 0.1 A cm^{-2} (3,137 s), the 0.05 A cm^{-2} time profile was significantly shortened to 1.63 times than that of 0.1 A cm^{-2}. To further complicate the problem, the FeS_2 cathode degradation and self-discharge not only decrease the specific capacity but also can trigger unexpected side reactions as well. To observe the composition of the electrodes, the cross-sectional SEM analysis and EDS mapping were conducted to investigate the by-products (Figure S1). From the image, a thin line was observed in the electrolyte region. Through the EDS analysis (mapping in Figure S1B), the thin line was composed of Li_2S byproduct along with K, Cl, and Fe.

There are two possible explanations for the sulfur ion generation. The long discharge period and exposure to heat can effectively degrade FeS_2 cathode, as stated in Eq. (2). Also, the long discharge period can facilitate the self-discharge reaction (Eq. (3)) that the generated sulfur gas can react with a dissolved sulfur anion to create polysulfide.[13e,14] The detection of Fe in the electrolyte supports this result, implying that self-discharge played a critical role in enriching the electrolyte with sulfur anion. Moreover, the polysulfide can enhance the sulfur gas dissolution into the electrolyte as well. All the dissociated sulfur ions can migrate to the electrolyte region and combine with the Li ions to generate Li_2S byproduct.[15] The continuous generation of Li_2S inherently reduced the capacity by decreasing the total amount of Li present in the system and increased the resistance in electrolyte; thus, the Li_2S ionic conductivity only showed 8×10^{-2} S cm^{-1} whereas LiF–LiCl–LiBr exhibited 0.24 S cm^{-1} at 25 °C.[11,16] Along with the Li_2S generation, there were other cube-like KCl byproduct crystals, as shown in Figure S1C–S1D. The reasonable explanation for the formation of KCl could be due to the formation of J-phase ($LiK_6Fe_{24}S_{26}Cl$ + Fe) and X phase ($13Li_2FeS_2 + 11\ Fe + 6\ K^+ + Cl^-$) in the cathode. The dissociated potassium ions could migrate toward the electrolyte and react with abundant chloride ions to form KCl crystals.[17] This reaction could also lead to depletion of salt in the cathode and hinder Li-ion movement resulting in higher resistance and lower capacity.

2.5. Comparison Between the Pure Li Anode with Li–Si Alloy Anode

The discharge comparison between the Li–Si alloy and pure Li anode is shown in Figure 6A and summarized in Table 3.

To make a precise comparison, the same amounts of electrolyte and cathode were used for two types of anodes. According to Equation (4), the Li–Si alloy exhibits several phase shifts during discharge; for this experiment, the first phase transition, $Li_{3.25}Si \rightarrow Li_{2.33}Si$, was only used to evaluate the discharge performance. The theoretical capacity of this particular region was 1,747 As g^{-1};[2] however, to increase the ionic conductivity, mechanical durability, and Li diffusivity of the

Table 3. Discharge results of Li anode and Li–Si anode single cell of the cut-off voltage (1.6 V) at 500 °C.

Anode type	Thickness [mm]	OCV [V]	Specific capacity [As g^{-1}]	Volumetric energy density [Wh l^{-1}]	Mass energy density [Wh kg^{-1}]
Li	0.61	2.06	1,469	251.4	59.3
Li–Si	2.0	1.93	574.8	122.5	21.0

© 2020 Wiley-VCH GmbH

25666223, 2021, 2, Downloaded from https://chemistry-europe.onlinelibrary.wiley.com/doi/10.1002/batt.202000211 by University of Ulsan, Wiley Online Library on [11/11/2025]. See the Terms and Conditions (https://onlinelibrary.wiley.com/terms-and-conditions) on Wiley Online Library for rules of use; OA articles are governed by the applicable Creative Commons License

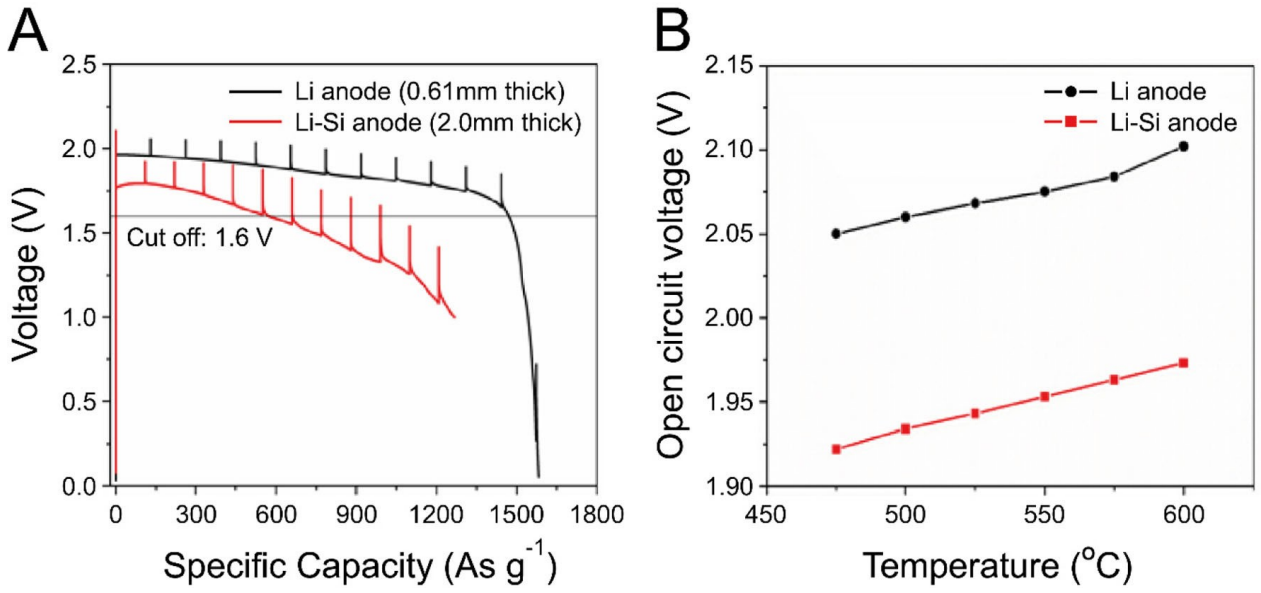

Figure 6. A) Discharge performance of Li anode and Li–Si anode single cell under 0.4 A cm^{-2} and 500 °C, B) OCV of a single cell with Li anode and Li–Si anode measured at various temperatures.

anode, 25% of LiCl–KCl eutectic salt was added to the anode, which decreased the theoretical specific capacity to 1,310 As g^{-1}.

$$Li_{3.25}Si \rightarrow Li_{2.33}Si \rightarrow Li_{1.71}Si \quad (4)$$

The open-circuit potential of Li–Si was 1.93 V, and at the cut-off voltage, the specific capacity only showed 574.8 As g^{-1}. Li anode, on the other hand, showed 2.06 V at OCV and the specific capacity of 1,469 As g^{-1} at the cut-off voltage, 2.5 times higher than that of Li–Si anode. Also, when comparing the energy density, the pure Li (254.1 Wh l^{-1}) showed twice the performance than the Li–Si anode (122.5 Wh l^{-1}). Due to the increase in resistance during the pulse intervals, the exact location where the phase shift of Li–Si occured was inconclusive. The sharp voltage drop of Li anode near the end of discharge suggests that all the Li ions traveled to FeS_2 cathode, showing higher ionic diffusivity compared to the Li–Si anode. In order for Li–Si anode to show similar discharge performance, two or more cells were required to deliver the same voltage and performance.

In Figure 6B, the temperature-dependent changes in open-circuit potential between pure Li and Li–Si anodes were investigated. For Li–Si, OCV increased from 1.92, 1.93, and 1.97 V for the temperatures at 475, 500, and 600 °C, respectively. The following temperature-dependent OCV change can be represented by Equation (5). This relationship [Eq. (6)] was also studied by previous reports by Bernardi et al.,[18] Chen et al.,[19] and Tomczuk et al.,[20] and the similarity between the voltage change rate, and the two equations suggests high credibility of the acquired data.

$$OCV = 1.73635\ (V) + 0.000393T\ (T : Celsius) \quad (5)$$

$$OCV = 1.612629\ (V) + 0.000405T\ (T : Kelvin) \quad (6)$$

Similar to the Li–Si anode, OCV change of the pure Li anode was also investigated. The change in OCV in pure Li anode was 2.05 V, 2.06 V, 2.10 V for the temperatures at 475 °C, 500 °C, and 600 °C, respectively. According to Guidotti et al., Li vs. Li–Al and Li–Si vs. FeS_2 system potentials were investigated, but the Li vs. FeS_2 system has not been examined yet.[2] Thus, to the authors' best knowledge, we are the first to propose the change in OCV with respect to the temperature for the Li vs. FeS_2 system to predict the voltage at a certain temperature for optimization of thermal batteries at different temperature requirements [Figure 6B, Eq. (7)].

$$OCV = 1.87073\ (V) + 0.000376T\ (T : Celsius) \quad (7)$$

The EIS Nyquist plot analysis was conducted to investigate the difference in resistance between the pure Li anode and Li–Si (Figure 7A–C). The temperature was set at 500 °C for this experiment. As mentioned above, the three discharge points, i.e., OCV, third pulse, and sixth pulse, were selected. The major difference between the pure Li and Li–Si was that the ohmic resistance was significantly higher, implying that even initial resistance itself was higher than the pure Li anode. Since the resistance arising from the assembly and electrolyte was almost identical for both electrodes, it is safe to assume that the higher resistance came from the anode exclusively. As shown in Figure 7A–C, the semicircle of Li–Si anode was significantly larger than that of the pure Li anode. This phenomenon could be related to interfacial charge transfer that the Li anode is inherently liquid in nature, whereas Li–Si is a solid. As the discharge occurs, the Li ion must travel longer distance due to the thickness of Li–Si anode, increasing the overall resistance. Another important factor to consider is the phase shift. Also

© 2020 Wiley-VCH GmbH

25666223, 2021, 2, Downloaded from https://chemistry-europe.onlinelibrary.wiley.com/doi/10.1002/batt.202000211 by University of Ulsan, Wiley Online Library on [11/11/2025]. See the Terms and Conditions (https://onlinelibrary.wiley.com/terms-and-conditions) on Wiley Online Library for rules of use; OA articles are governed by the applicable Creative Commons License

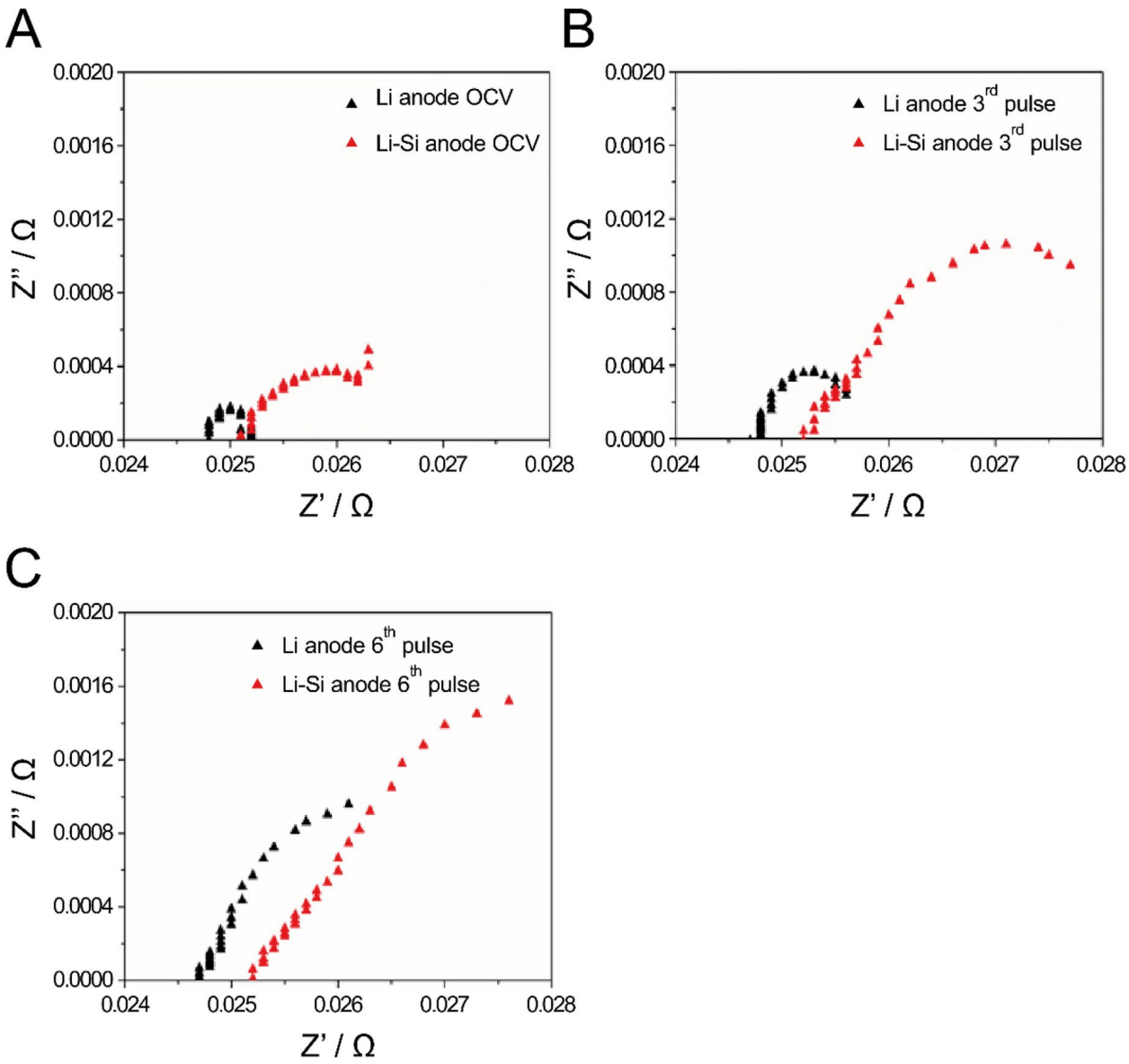

Figure 7. Electrochemical impedance spectroscopy of Li anode and Li–Si anode single cells at 500 °C A) OCV, B) third pulse OCV, and C) sixth pulse OCV.

observed in the discharge profile in Figure 6A, the phase shift resulted in lower voltage and high resistance, which resulted in a higher semicircle for the EIS analysis.

2.6. Li Anode Thermal Battery Discharge Performance

Based on the previous results, the thermal batteries with 17 cells (13 wt% Li anode) under 4 kgf cm^{-2} applied pressure were built to test the actual thermal battery operation performance. The applied current density was 0.3 A cm^{-2}. The thermal batteries were discharged at low (−32 °C) and high (63 °C) temperatures abiding by the typical military operating temperature requirements. The heat pellet was designed so that the internal temperature of the thermal battery was over 450 °C for low temperature and lower than 550 °C for high-temperature discharge.

The experiments did not show voltage fluctuation or short circuit, suggesting no Li leakage during discharge in Figure 8. The thermal batteries discharged at low and high temperatures showed an open-circuit potential of 34.8 V (2.047 V per cell) and 35.1 V (2.065 V per cell), respectively (Table 4).

This result coincides with the previous results, indicating that higher temperatures result in the higher voltage; furthermore, the voltage was higher throughout the entire discharge for the thermal battery discharged at 63 °C. With 27.2 V cut-off (1.6 V per cell), the specific capacities of the low and high thermal batteries are 1,473 A s g^{-1} (79.0 % utilization) and 1,386 A s g^{-1} (76.7 % utilization), respectively. To investigate the change in the cell after discharge and the underlying reason for capacity loss in the high-temperature thermal battery, two thermal batteries were disassembled, and the ninth cells were taken as samples. The cross-sectional image and EDS analysis were conducted, and the results are shown in Figure S2 and S3

© 2020 Wiley-VCH GmbH

25666223, 2021, 2, Downloaded from https://chemistry-europe.onlinelibrary.wiley.com/doi/10.1002/batt.202000211 by University of Ulsan, Wiley Online Library on [11/11/2025]. See the Terms and Conditions (https://onlinelibrary.wiley.com/terms-and-conditions) on Wiley Online Library for rules of use; OA articles are governed by the applicable Creative Commons License

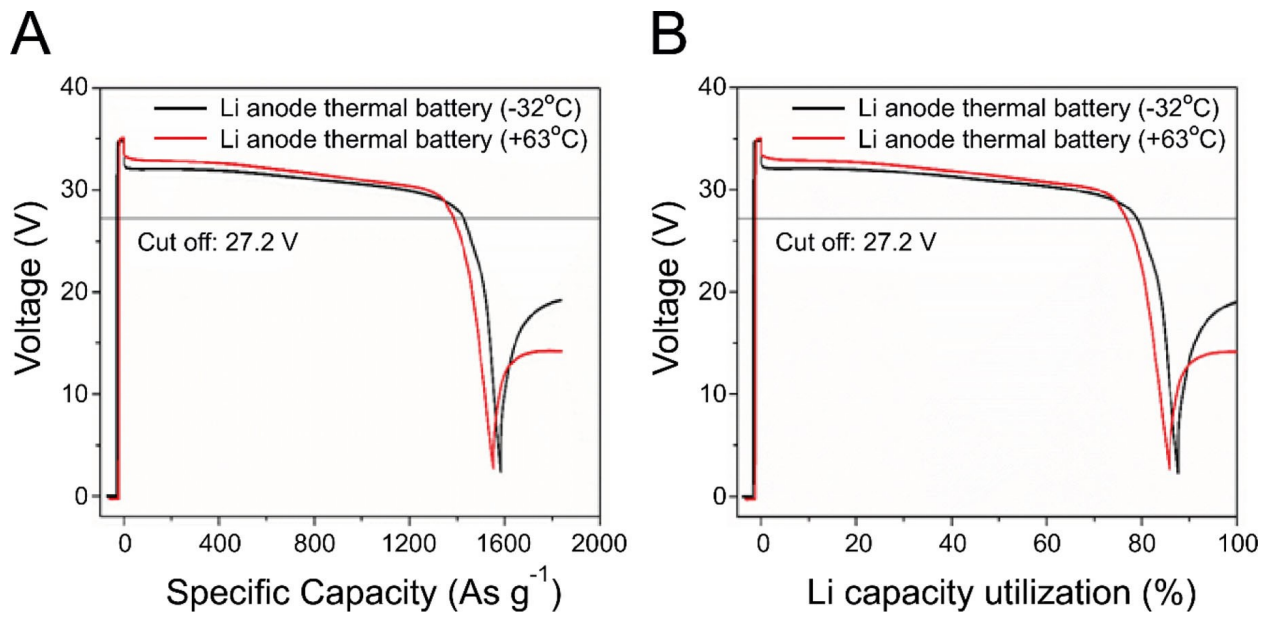

Figure 8. A) Discharge test results and specific capacity of thermal batteries with 17 Li anode cells at low temperature (−32 °C) and high temperature (63 °C) and B) Li anode utilization.

Table 4. Discharge results of Li anode thermal battery under low and high temperature.

Test condition	OCV [V]	Cut-off voltage (27.2 V) Specific capacity [As g^{-1}]	Li capacity utilization [%]
Low temperature (−32 °C)	34.8 (2.047 per cell)	1,427	79.0
High temperature (63 °C)	35.1 (2.065 per cell)	1,386	76.7

for high and low-temperature thermal battery cells, respectively. Both cells showed that there were some unreacted FeS_2 active ingredients near the heat source, confirming that excess amount of cathode was provided for both batteries. Figure S2A illustrates a thin line in the electrolyte layer; the EDS analysis revealed that this layer consists of Li_2S byproducts (Figure S2B). However, this phenomenon was not observed in the low-temperature discharge (Figure S3A–C). As mentioned above, the sulfur anion was generated via degradation of FeS_2 cathode and self-discharge reaction, resulting in the decreased specific capacity for the high-temperature thermal battery discharge.

3. Conclusions

The electrochemical properties of pure Li anode were investigated with respect to different Li loading, applied pressure, temperatures, and current densities. The comparison between the as-processed Li anode and Li–Si anode demonstrated the superior performance (approximately two times larger in both specific capacity and energy density), suggesting the practical utilization of Li anode in the future weapon systems.

The compiled results are: 15 wt% Li or below, 6 kgf cm^{-2} or below, 500 °C, and 0.2–0.4 A cm^{-2} for Li loading, applied pressure, discharge temperature, and current density range, respectively. Based on these results, two thermal batteries with 17 cells were manufactured and discharged at low (−32 °C) and high (63 °C) temperature to further confirm the validity of the results. Both thermal batteries showed anticipated results, suggesting that the conclusion drawn in this experiment is compelling.

This study proposed a holistic approach to optimizing Li-based thermal battery cells. The anodic performance was extensively studied to provide a guideline for optimizing the thermal battery performance. It should be emphasized that anodic performance alone should not be considered because the overall cell performance depends on the other constituents as well. The guideline provided here should contribute to the development of future thermal batteries.

For future work, the discharge performance comparison with other alloys such as Li–B should be considered to demonstrate how other thermal battery anodes perform when compared to the Li anode. Also, the novel, lighter material that can prohibit the lithium leakage is also in demand in the field of thermal battery technology in order to increase both lithium loading and specific energy (volume and mass).

© 2020 Wiley-VCH GmbH

25666223, 2021, 2, Downloaded from https://chemistry-europe.onlinelibrary.wiley.com/doi/10.1002/batt.202000211 by University of Ulsan, Wiley Online Library on [11/11/2025]. See the Terms and Conditions (https://onlinelibrary.wiley.com/terms-and-conditions) on Wiley Online Library for rules of use; OA articles are governed by the applicable Creative Commons License

Acknowledgment

This work was supported by the Agency for Defense Development (ADD) in South Korea.

Conflict of Interest

The authors declare that they have no known competing financial interests or personal relationships that could have appeared to influence the work reported in this paper.

Keywords: thermal batteries · Li anode · optimization · discharge performance · operational safety

[1] a) R. A. Guidotti, P. Masset, *J. Power Sources* **2006**, *161*, 1443–1449; b) C. N. Im, *J. Korean Inst. Electr. Electron. Mater. Eng.* **2017**, *30*, 318–324.
[2] R. A. Guidotti, P. J. Masset, *J. Power Sources* **2008**, *1*, 388–398.
[3] a) G. C. Bowser, J. R. Moser, U. S. Patent 3,930,888, **1976**; b) D. E. Harney, U. S. Patent 4,221,849, **1980**; c) J. H. Cho, C. N. Im, C. H. Choi, S. H. Ha, H. K. Yoon, Y. Choi, J. Bae, *Electrochim. Acta* **2020**, *353*, 136612; d) S. H. Wang, J. Yue, W. Dong, T. T. Zuo, J. Y. Li, X. Liu, X. D. Zhang, L. Liu, J. L. Shi, Y. X. Yin, *Nat. Commun.* **2019**, *10*, 1–8.
[4] Y. S. Choi, H. R. Yu, H. W. Cheong, *J. Power Sources* **2015**, *276*, 102–104.
[5] a) J. D. Briscoe, E. Durliat, F. Salver-Disma, I. Stewart, in *42nd Power Sources Conference*, **2006**, p. 117–120; b) A. Clark, C. Thaler, I. Stewart, J. Reid, in *39th Power Sources Conference*, **2000**.
[6] a) D. Jeppson, J. Ballif, W. Yuan, B. Chou, *Lithium Literature Review: Lithium's Properties and Interactions*, Hanford Engineering Development Lab, **1978**; b) S. Krat, A. Popkov, Y. M. Gasparyan, A. Pisarev, P. Fiflis, M. Szott, M. Christenson, K. Kalathiparambil, D. N. Ruzic, *Fusion Eng. Des.* **2017**, *117*, 199–203; c) J. Wang, H. Wang, J. Xie, A. Yang, A. Pei, C. L. Wu, F. Shi, Y. Liu, D. Lin, Y. Gong, *Energy Storage Mater.* **2018**, *14*, 345–350.
[7] S. Fujiwara, M. Inaba, A. Tasaka, *J. Power Sources* **2011**, *196*, 4012–4018.
[8] C. N. Im, H. K. Yoon, T. Y. Ahn, J. S. Yeo, S. H. Ha, H. R. Yu, S. Baek, J. H. Cho, *Appl. Chem. Eng.* **2018**, *29*, 696–702.
[9] C. N. Im, T.-Y. Ahn, H. R. Yu, S. H. Ha, J. S. Yeo, J. H. Cho, H. J. Yoon, *J. Korean Inst. Electr. Electron. Mater. Eng.* **2019**, *32*, 165–173.
[10] P. J. Masset, R. A. Guidotti, *J. Power Sources* **2008**, *177*, 595–609.
[11] P. Masset, R. A. Guidotti, *J. Power Sources* **2007**, *164*, 397–414.
[12] a) S. H. Kang, S. H. Chae, H. W. Cheong, K. H. Kim, Y. S. Han, S. M. Lee, D. H. Yoon, J. Yi, *Ceram. Int.* **2017**, *43*, 4023–4028; b) J. Pemsler, R. Lam, J. Litchfield, S. Dallek, B. Larrick, B. Beard, *J. Electrochem. Soc.* **1990**, *137*, 1–7.
[13] a) Y. Choi, H. R. Yu, H. Cheong, S. Cho, Y. S. Lee, *Appl. Chem. Eng.* **2014**, *25*, 161–166; b) D. Andre, M. Meiler, K. Steiner, H. Walz, T. Soczka-Guth, D. Sauer, *J. Power Sources* **2011**, *196*, 5349–5356; c) Y. Choi, S. Cho, Y. S. Lee, *J. Ind. Eng. Chem.* **2014**, *20*, 3584–3589; d) P. Singh, R. A. Guidotti, D. Reisnerc, *J. Power Sources* **2004**, *138*, 323–326; e) R. A. Guidotti, F. W. Reinhardt, J. A. Smaga, in *Proceedings of the 34th International Power Sources Symposium*, **1990**, p. 132–135; f) J. S. Yeo, J. H. Lee, E. J. Yoo, *Electrochim. Acta* **2018**, *290*, 228–235.
[14] a) S. Schoeffert, *J. Power Sources* **2005**, *142*, 361–369; b) D. Linden, T. B. Reddy, *Handbook of Batteries*, McGraw-Hill, New York, **2002**.
[15] a) S. S. Wang, R. N. Seefurth, *J. Electrochem. Soc.* **1987**, *134*, 530; b) B. J. Burrow, K. W. Nebesny, N. R. Armstrong, R. K. Quinn, D. E. Zurawski, *J. Electrochem. Soc.* **1981**, *128*, 1919.
[16] T. Hakari, A. Hayashi, M. Tatsumisago, *Chem. Lett.* **2015**, *44*, 1664–1666.
[17] a) D. Bernardi, E. M. Pawlikowski, J. Newman, *J. Electrochem. Soc.* **1988**, *135*, 2922–2931; b) Z. Tomczuk, S. Preto, M. Roche, *J. Electrochem. Soc.* **1981**, *128*, 760; c) Z. Tomczuk, B. Tani, N. Otto, M. Roche, D. Vissers, *J. Electrochem. Soc.* **1982**, *129*, 925–931.
[18] D. Bernardi, J. Newman, *J. Electrochem. Soc.* **1987**, *134*, 1309–1318.
[19] K. S. Chen, G. H. Evans, R. S. Larson, D. R. Noble, W. G. Houf, *Final Report on LDRD Project: A Phenomenological Model for Multicomponent Transport with Simultaneous Electrochemical Reactions in Concentrated Solutions*, Sandia National Labs, **2000**.
[20] Z. Tomczuk, D. Vissers, *J. Electrochem. Soc.* **1986**, *133*, 2505–2509.

Manuscript received: September 8, 2020
Revised manuscript received: October 5, 2020
Version of record online: November 17, 2020

© 2020 Wiley-VCH GmbH

25666223, 2021, 2, Downloaded from https://chemistry-europe.onlinelibrary.wiley.com/doi/10.1002/batt.202000211 by University of Ulsan, Wiley Online Library on [11/11/2025]. See the Terms and Conditions (https://onlinelibrary.wiley.com/terms-and-conditions) on Wiley Online Library for rules of use; OA articles are governed by the applicable Creative Commons License